Journal of Functional Materials and Applied Engineering

Research Paper

Preparation and Properties of Agarose-Locust Bean GumHydrated Salt Eutectic Form-Stable Phase Change Materials

David S. Hesman[1], Robert E.Masuoka[2], Edward J. Wolfe[2,*]

[1] Faculty of Architecture, Civil Engineering and Urban Planning, Brandenburg University of Technology, Cottbus, Brandenburg, Germany
[2] University of Canberra, University Dr, Bruce ACT 2617, Australia
*Corresponding author: DHesman@b-tu.de; RobertEM@canberra.edu.au; ejw@canberra.edu.au

Abstract. A binary eutectic salt mixture comprising $Na_2SO_4·10H_2O$ (SSD) and $Na_2HPO_4·12H_2O$ (SPDD) was initially dispersed in water to mitigate phase segregation within the system. Thereafter, $Na_2SiO_3·9H_2O$ (SMN) was introduced as a nucleating agent to markedly diminish the supercooling degree of the resulting SSD/SPDD/H_2O/SMN composite phase change material. Finally, an agarose-locust bean gum (AG-LBG)/hydrated salt eutectic form-stable phase change material (SSD/SPDD/H_2O/SMN/AG-LBG) was obtained by impregnating the three-dimensional network structure of AG-LBG with SSD/SPDD/H_2O/SMN. The optimal mass ratio of SSD/SPDD salt mixture was determined by DSC analysis, the optimal nucleating agent as well as its addition amount were determined by step cooling test, while the optimal m(AG):m(LBG) and the optimal loading capacity of SSD/SPDD/H_2O/SMN onto the AG-LBG supporting skeleton were determined based on leakage test and simulated working condition experiment. The results showed that the phase transition temperature and enthalpy of the SSD/SPDD mixture prepared with m(SSD):m(SPDD)=52:48 by physical composite were 28.90 °C and 216.40 J/g, respectively. The SSD/SPDD/H_2O/SMN phase change system prepared by water addition amount (based on the mass of SSD/SPDD salt mixture, the same below) of 13% and SMN addition amount of 3% displayed the lowest supercooling degree of 0.16 °C, and of 0.18 °C after 60 cold and hot cycles. The optimal m(AG):m(LBG) ratio of AG-LBG supporting skeleton was 75:25, and the optimal loading capacity of SSD/SPDD/H_2O/SMN phase change system was 85%. The obtained best form-stable phase change material (SSPCM) could maintain 80 min without leakage under the above-mentioned conditions. The SSPCM displayed a melting point of 26.40 °C, an enthalpy of fusion of 147.20 J/g, and a thermal conductivity of 0.11 W/(m·K). Thermal insulation simulations conducted under identical conditions revealed that, in comparison with the foam sandwich reference, the SSPCM-integrated building envelope prolonged the core temperature rise duration by a factor of 2.60 during the heating phase, while the cooling period was extended by 1.37 times.

Keywords: *agarose; locust bean gum; hydrated salt; phase separation; building insulation; functional materials*

Received on 10 Apr 2022, Accepted on 15 June 2022, Published on 08 July 2022

1 Introduction

In contemporary society, energy consumption and environmental pollution stand as pivotal challenges constraining the sustainable development of humanity [1–3]. The construction industry, consuming over one-third of global total energy, represents the largest energy-consuming sector worldwide [4]. Consequently, developing novel technologies to enhance building energy efficiency and flatten energy consumption profiles [5] has become a global research priority. Among various emerging technologies, thermal energy storage (TES) is recognized as a highly effective approach to improving energy efficiency [6]. TES resolves the spatiotemporal constraints of thermal energy, bridging the gap between energy demand and supply. Applying TES technology to the building sector can reduce energy consumption and improve indoor thermal comfort [7–8]. TES technologies are broadly categorized into sensible heat storage, latent heat storage, and chemical reaction storage [9]. Among these approaches, latent heat storage utilizing phase change materials (PCMs) is considered the most effective thermal energy storage technology, owing to its straightforward operation, narrow temperature variation during phase transition, and substantial energy storage density [10]. Driven by the continuous advancement of PCMs,

latent heat thermal storage technology is gaining increasing attention for building temperature regulation applications [11–12].

Compared with organic PCMs, inorganic hydrated salts possess outstanding advantages including large heat storage capacity, low cost, abundant sources, non-toxicity, and non-flammability. Therefore, hydrated salts have attracted significant attention for their excellent performance and broad prospects in thermal management applications, emerging as a research hotspot in the field of thermal storage, particularly for building thermal management [13]. In reported studies, single PCMs with phase transition temperatures falling within the human comfort zone are generally used directly for building temperature control [14]. However, few hydrated salts exhibit phase transition temperatures that meet the requirements for indoor thermal comfort (18–32 °C) [15]. Thus, two or more hydrated salts must be melted and mixed to form eutectic molten salts, thereby broadening the applicable phase transition temperature range. Compared with single molten salts, eutectic molten salts offer advantages such as good stability and controllable phase transition temperature [16]. $Na_2SO_4·10H_2O$ is a widely available, low-cost hydrated salt with high energy storage density, holding good potential for building applications [17]. Nevertheless, its phase transition temperature of 32.40 °C is slightly higher than the requirement for thermal comfort [18]. Therefore, in practical applications, it is often compounded with other hydrated salts to form eutectic molten salts with lower phase transition temperatures. SANG et al. [18] employed a eutectic molten salt system comprising sodium sulfate decahydrate and sodium carbonate decahydrate as the phase change material, with sodium polyacrylate incorporated to prevent phase segregation. Borax was introduced as a nucleating agent, reducing the supercooling degree to 3.20 °C. The addition of flake graphite enhanced thermal conductivity to 0.819 W/(m·K), while the phase transition temperature was modulated to 22.40 °C—a substantial reduction relative to pure sodium sulfate decahydrate (32.40 °C). Inorganic hydrated salts exhibit considerable potential for practical applications and favorable cost benefits as PCMs; however, they are generally plagued by common drawbacks including phase separation, supercooling, and leakage during solid–liquid transitions. Phase separation is primarily caused by the sedimentation of high-density residual salts at the bottom [16]. Some hydrated salts exhibit low solubility; after losing crystallization water, the density difference between solid inorganic salts and the solution becomes significant, leading to the settlement of solid particles and stratification, which worsens with increasing melting and solidification cycles. This issue can be mitigated by adding thickening agents. Supercooling refers to a phenomenon where a PCM in a metastable state does not crystallize upon reaching its solidification temperature; crystallization only initiates after further temperature reduction [19]. Currently, one of the most effective methods to resolve supercooling is adding nucleating agents, termed "seed crystals," which are substances with crystal structures similar to the heat storage material in terms of lattice spacing [20]. Furthermore, the leakage problem of inorganic hydrated salts during phase transitions also restricts their further application in the building sector.

To mitigate the inherent limitations of inorganic hydrated salts—including phase segregation, supercooling, leakage, and elevated thermal conductivity—while simultaneously accounting for chemical stability, operational safety, and economic feasibility, the present work proposes a design strategy grounded in the phase transition mechanism whereby solid inorganic salts within the hydrate are capable of redissolving into the liberated crystallization water upon melting. Specifically, the water content in the system is increased to enable partially undissolved solid inorganic salts to overcome the interionic attractive forces on the crystal lattice surface, completely dissolve in water, and recombine with polar water molecules to form hydrated ions, fundamentally resolving the phase separation challenge. The present study proposes to employ $Na_2SO_4·10H_2O$ and $Na_2HPO_4·12H_2O$ as the primary phase change constituents for the preparation of a form-stable PCM, with the objective of reducing the phase transition temperature through binary eutectic formation. A small amount of H_2O is added to alleviate phase separation and further reduce the PCM usage cost. Nucleating agent $Na_2SiO_3·9H_2O$ is incorporated to reduce supercooling. The three-dimensional network structure of agarose-locust bean gum (AG-LBG), a naturally derived, non-toxic, and safe polysaccharide, is utilized as the supporting skeleton to eliminate supercooling, reduce thermal conductivity, and resolve the leakage problem simultaneously. Thermal buffering performance of the prepared form-stable PCM is evaluated via insulation simulation tests, aiming to provide references for PCM preparation in building thermal insulation applications.

2 Experimental Section

2.1 Reagents and Instruments

Sodium sulfate decahydrate, sodium hydrogen phosphate dodecahydrate, sodium silicate nonahydrate, locust bean gum, and sodium acetate trihydrate were of analytical grade and sourced from Shanghai Aladdin Biochemical Technology Co., Ltd. Agarose (analytical grade) was purchased from Beijing Solarbio Science & Technology Co., Ltd. Borax was obtained from Sinopharm Chemical Reagent Co., Ltd. The TP700 multi-channel data logger was acquired from Shenzhen Toprie Electronics Co., Ltd., and the SB manual sample preparation machine from Xiangtan Xiangyi Instrument Co., Ltd. The Nicolet™ iN 10 infrared microscope and Axia Chemi scanning electron microscope (SEM) were procured from Thermo Fisher Scientific (USA). DSC3500 differential scanning calorimeter (DSC) was purchased from TA Instruments, USA. SmartLab 9 X-ray diffractometer (XRD) was purchased from Rigaku Corporation, Japan. FDM-2000 freeze dryer was purchased from Eyela, Japan. LFA 467 HyperFlash laser flash apparatus was purchased from Netzsch, Germany.

2.2 Methods

2.2.1 Theoretical Calculation

The Schroeder equation elucidates the correlation between the thermophysical properties of eutectic constituents across varying compositions [21]. Equations (1) and (2) were employed to estimate the theoretical eutectic temperature and the associated phase transition enthalpy:

$$Tm=[Ti1-R\Delta Hm,ilnXi]-1 \quad (1)$$

$$Hm=Teu\sum[TiXiHi+\{Xi(Cp,li-Cp,si)lnTiTeu\}] \quad (2)$$

Where irepresents SSD and SPDD; T_m(T_eu) denotes the phase transition temperature of the eutectic mixture, expressed in Kelvin; T_i represents the phase transition temperature of individual hydrated salt component i, in Kelvin; X_i indicates the mole fraction of component i within the eutectic system, in percent; ΔH_m,i(H_i) corresponds to the melting enthalpy of component i, in Joules per mole; R is the universal gas constant, 8.314 J/(mol·K); C_p,li and C_p,si signify the specific heat capacities of component i in the liquid and solid phases, respectively, in Joules per gram per Kelvin. Based on the above equations, the melting points were calculated for m(SSD):m(SPDD) ratios of 100:0, 90:10, 80:20, 70:30, 60:40, 50:50, 40:60, 30:70, 20:80, 10:90, and 0:100 to draw the phase diagram, determining the theoretical eutectic mass ratio and corresponding eutectic melting point. Theoretical calculation results were further validated by DSC testing to ensure reliability.

2.2.2 Preparation of Phase Change System

Based on theoretical calculation results, binary mixed salts with m(SSD):m(SPDD) ratios of 51:49, 52:48, 53:47, 54:46, 55:45, 56:44, 57:43, 58:42, and 59:41 were prepared. 10.00 g of SSD and SPDD were accurately weighed and transferred into a 20 mL glass vial. The mixture was melted in a thermostatic water bath maintained at 50 °C for 1 h, followed by magnetic stirring for an additional 1 h to ensure thorough homogenization, thereby producing SSD/SPDD mixed salts with varying mass ratios of m(SSD):m(SPDD) ratios. Based on DSC test results, SSD/SPDD mixed salt with m(SSD):m(SPDD)=52:48 was selected as the eutectic system; 13% H_2O and 3% SMN were added to prepare the SSD/SPDD/H_2O/SMN phase change system.

Following the same procedure, SMN was replaced with borax or SAT to prepare SSD/SPDD/H_2O/borax and SSD/SPDD/H_2O/SAT phase change systems, respectively.

2.2.3 Preparation of Form-Stable PCM System

First, AG and LBG composite hydrogels were prepared. AG and LBG were weighed according to m(AG):m(LBG) = 75:25, specifically 0.338 g AG and 0.112 g LBG. They were then added to a 20 mL glass vial, followed by the addition of 14.55 g deionized water. The mixture was heated and stirred in an 85 °C water bath for 30 min, then cooled to room temperature to obtain a stable AG-LBG hydrogel. The hydrogel was pre-frozen in a refrigerator at –17 °C for 12 h, followed by freeze-drying (–86 °C, 36 h) to obtain the AG-LBG skeleton, denoted as AG-LBG (75/25).

Following the same procedure, the m(AG):m(LBG) ratio was adjusted to prepare AG-LBG skeletons denoted as AG-LBG (100/0), AG-LBG (50/50), and AG-LBG (25/75) for m(AG):m(LBG) ratios of 100:0, 50:50, and 25:75, respectively.

The form-stable PCM system was prepared via the impregnation method. Molten SSD/SPDD/H_2O/SMN phase change system (2.20, 2.55, and 3.01 g) was sampled in batches using a 1 mL rubber dropper and added dropwise into the AG-LBG skeleton. Leakage characterization was performed to establish the maximum phase change material loading capacity of the supporting matrix. Composite PCM formulations with PCM mass fractions of 83%, 85%, and 87% were fabricated and subjected to thermal exposure in a 50 °C oven for 2 h to evaluate leakage propensity. The optimal SSD/SPDD/H_2O/SMN/AG-LBG form-stable PCM system was denoted as SSPCM.

2.3 Characterization Methods and Performance Testing

2.3.1 Step Cooling Curve Test

10 g of sample was placed in a 20 mL sample vial, and the temperature recorder probe was fixed at the center of the sample until the temperature stabilized. Subsequently, the sample was transferred to an ice-water bath, and the temperature was recorded every 1 s using a multi-channel temperature recorder to plot the step cooling curve.

2.3.2 Characterization Methods

FTIR characterization was carried out in attenuated total reflectance mode over the 4000–500 cm^{-1} interval at a spectral resolution of 4 cm^{-1}, with each spectrum comprising 32 co-added scans. XRD analysis was conducted using a copper target operated at 40 kV and 40 mA, with Kα radiation (λ = 0.1541 nm) and a scanning rate of 5°/min across a 2θ range of 5°–80°. For SEM observation, specimens were sputter-coated with gold and examined in low-vacuum secondary electron mode at a beam current of 20 μA and an accelerating voltage of 10 kV. DSC measurements were performed under a nitrogen atmosphere, covering a temperature range of –20 to 65 °C with heating and cooling rates of 5 °C/min.

2.3.3 Leakage Test

Three grams of the solidified SSD/SPDD/H_2O/SMN system were compressed into a disc specimen with 2.5 cm diameter and 2.0 mm thickness using a manual pellet press. An equivalent mass of SSPCM was similarly compacted into a disc of identical dimensions. Specimens were initially positioned on filter paper, then transferred together with the filter paper into a clean petri dish, sealed with polymeric film, and subjected to thermal exposure in a 50 °C forced-air convection oven. A digital camera was used to record changes in PCM shape at different times.

2.3.4 Thermal Conductivity Test

The thermal diffusivity (α, m^2/s) of the specimens was determined by means of a laser flash method. The specific heat capacity (Cp, J/(kg·K)) was determined by means of differential scanning calorimetry (DSC). The thermal conductivity (λ, W/(m·K)) was then calculated according to Equation (3):

$$\lambda=\alpha C p \rho \quad (3)$$

Where ρis the sample density, kg/m^3.

2.3.5 Simulated Working Condition Test

Referring to the testing method of Wang Xuan et al. [19] from our research group, three nested acrylic plates were designed to conduct heating and cooling performance tests with no filling, foam insulation board, or SSPCM in the interlayer. Heating tests were conducted in a 35 °C forced-air drying oven; cooling tests were conducted in a refrigerator (4 °C).

3 Results and Discussion

3.1 Determination of Eutectic Composition

Figure 1a shows the binary eutectic phase diagram of the SSD/SPDD mixed salt.
From Figure 1a, it can be seen that as the m(SSD):m(SPDD) ratio in the SSD/SPDD mixed salt decreases, the melting point of SSD gradually decreases, while that of SPDD gradually increases. The two curves exhibit continuous variation and ultimately converge at an intersection point, which corresponds to the eutectic point. At this eutectic point, the SSD–SPDD binary mixture undergoes simultaneous melting. Within the composition range where m(SSD):m(SPDD) varies from 60:40 to 50:50, the eutectic temperature is approximately 29 °C, which is lower than the melting points of the individual hydrated salts—SSD (34.7 °C) and SPDD (37.0 °C). This is because, in the mixed salt, the other salt acts as an impurity for either SSD or SPDD; the increasing relative content of impurities leads to increased entropy generation, thereby lowering the melting point of the mixture [22].

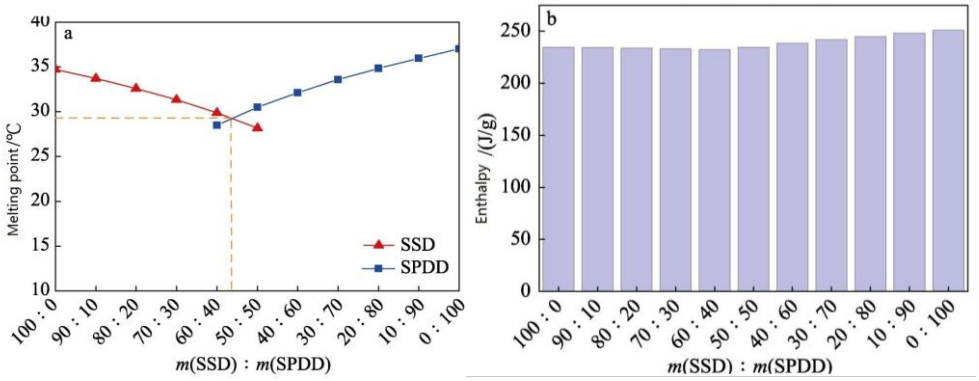

Figure 1 Phase diagram (a) and phase transition enthalpy value (b) of SSD/SPDD mixed salt binary eutectic

Figure 1b presents the phase transition enthalpy values for the SSD/SPDD binary eutectic mixture. The latent heat of phase transformation represents another critical parameter for eutectic phase change materials. As depicted in Figure 1b, the phase transition enthalpy at the SSD/SPDD eutectic composition ranges between 220 and 230 J/g.
Figure 2 shows the DSC curves of mixed salts with m(SSD):m(SPDD) ratios ranging from 51:49 to 59:41. Table 1 lists the phase transition temperatures and enthalpies.

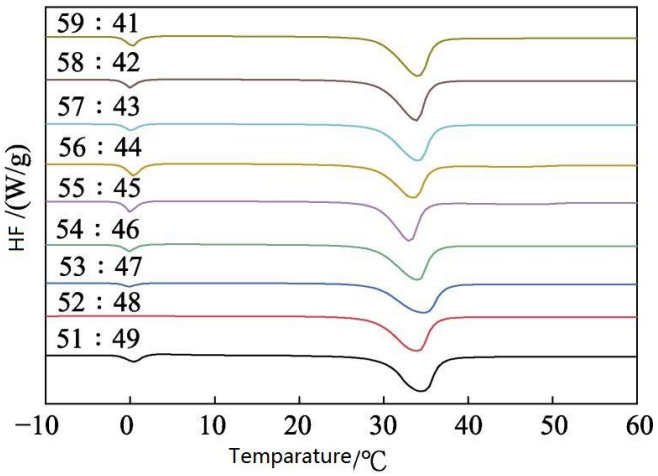

Figure 2 DSC curves of salt mixtures with m(SSD):m(SPDD) = 51:49 ~ 59:41

As illustrated in Figure 2, among the SSD/SPDD binary salt mixtures investigated, solely the formulation with a mass ratio of m(SSD):m(SPDD) = 52:48 displayed a single endothermic peak, whereas all other compositions exhibited dual peaks. This phenomenon may be rationalized by the progressively weakened interaction between

water molecules and salt ions within the hydrate as the temperature declines, whereby a fraction of the bound water is converted into free water that subsequently crystallizes at a characteristic temperature, thereby giving rise to an additional phase transition peak attributable to water. Therefore, it is inferred that the SSD/SPDD mixed salt with m(SSD):m(SPDD)=52:48 forms a eutectic. At this ratio, the mixed salt phase transition temperature is 28.90 °C (Table 1), consistent with the predicted result (29 °C), and the phase transition enthalpy is 216.40 J/g, slightly lower than the calculated value (220–230 J/g). This may be attributed to sampling errors in DSC testing, where the sample mass is 5–10 mg; for binary mixtures, achieving ideal homogeneity during mixing is difficult, leading to deviations. Therefore, SSD/SPDD mixed salt with m(SSD):m(SPDD)=52:48 (hereafter referred to as SSD/SPDD mixed salt) was selected as the optimal composition for subsequent studies.

Figure 3 shows the XRD patterns of SSD, SPDD, and the SSD/SPDD mixed salt.

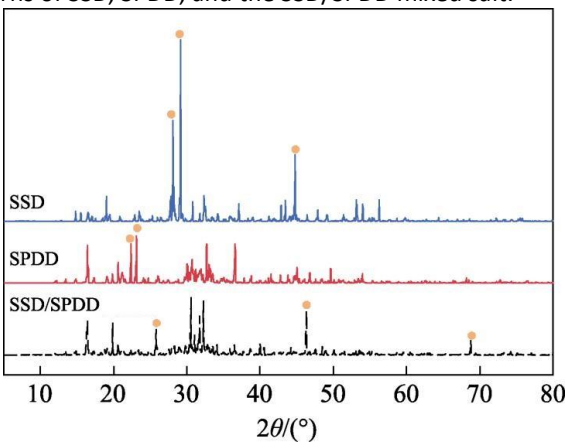

Figure 3 XRD patterns of SSD, SPDD and SSD/SPDD salt mixture

From Figure 3, it can be seen that compared with SSD and SPDD, the SSD/SPDD mixed salt exhibits new diffraction peaks at 2θ = 25.78°, 46.30°, and 68.62°. Meanwhile, the strong diffraction peaks of SSD at 2θ = 27.78°, 29.20°, and 44.60°, as well as the strong characteristic peaks of SPDD at 2θ = 22.24° and 23.15°, disappear or weaken in intensity in the mixed salt. This indicates that the diffraction peaks of the mixed salt are not a simple superposition of the two salts, confirming that SSD and SPDD have formed a eutectic.

Figure 4 shows the FTIR spectra of SSD, SPDD, and the SSD/SPDD mixed salt.

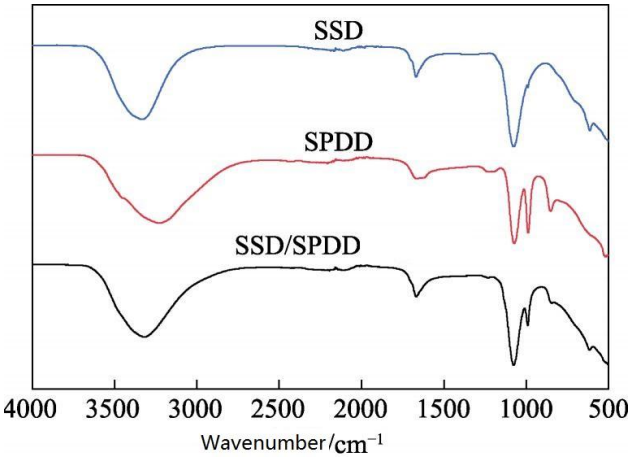

Figure 4 FTIR spectra of SSD, SPDD and SSD/SPDD salt mixture

As illustrated in Figure 4, SSD, SPDD, and their binary composite all exhibit absorption peaks in the 3600–2900 cm^{-1} and 1710–1605 cm^{-1} ranges, corresponding to the O–H stretching vibration and H–O–H bending vibration of water molecules, respectively. The SSD/SPDD mixed salt also preserves the characteristic absorption of SSD at 1080 cm^{-1} (asymmetric stretching vibration of SO_4^{2-}) and the characteristic peak of SPDD at 989 cm^{-1} (stretching vibration of the P–O bond). No new characteristic peaks appear in the SSD/SPDD mixed salt, indicating that it is formed via physical compounding rather than chemical reaction.

3.2 Phase Separation and Cycling Stability Analysis

Figure 5 shows digital photographs of the SSD/SPDD mixed salt and the SSD/SPDD mixed salt with 11%, 12%, and 13% water addition, after heating and stirring at 50 °C for 1 h followed by standing for 2 h.

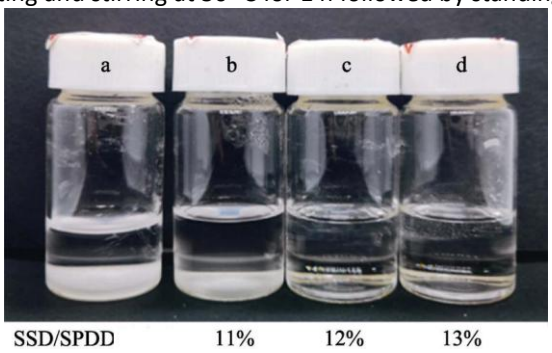

Figure 5 Digital photos of SSD/SPDD salt mixture (a) and SSD/SPDD salt mixture with water addition amount of 11% (b), 12% (c), 13% (d)

To resolve the phase separation issue of eutectic salts, a strategy of increasing the solubility of solid inorganic salts during phase transition was adopted by adding extra water to completely dissolve the precipitated salts. From Figure 5, it can be seen that adding 13% water completely eliminates the phase separation phenomenon. Figure 6 shows the digital photographs of the SSD/SPDD mixed salt with 13% water addition after 0 and 100 hot and cold cycles.

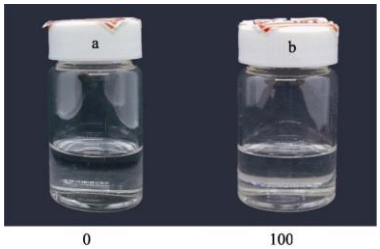

Figure 6 Digital photos of SSD/SPDD salt mixture with water addition amount of 13% after 0 (a) and 100 hot and cold cycles (b)

From Figure 6, it can be seen that after 100 hot and cold cycles, no obvious phase separation occurs, indicating that the SSD/SPDD mixed salt with 13% water addition possesses good stability. Hereafter, the SSD/SPDD mixed salt with 13% water addition is denoted as SSD/SPDD mixed salt/H_2O.

3.3 Screening of Nucleating Agents

Figures 7a and 7b show the step cooling curves and supercooling degrees of the SSD/SPDD/H_2O/SMN, SSD/SPDD/H_2O/borax, and SSD/SPDD/H_2O/SAT phase change systems.

From Figures 7a and 7b, it can be seen that the supercooling degree of SSD/SPDD mixed salt/H_2O without nucleating agent addition is 6.60 °C. The supercooling degrees of the SSD/SPDD/H_2O/SMN, SSD/SPDD/H_2O/borax, and SSD/SPDD/H_2O/SAT phase change systems with 3% addition of SMN, borax, and SAT are 0.20 °C, 2.50 °C, and 8.75 °C, respectively. Therefore, the SSD/SPDD/H_2O/SMN phase change system was selected for subsequent studies.

Figures 7c and 7d show the step cooling curves and supercooling degrees of the SSD/SPDD/H_2O/SMN phase change systems with 2%, 3%, and 4% SMN addition, respectively.

From Figures 7c and 7d, it can be seen that as the SMN addition amount (2%, 3%, and 4%) increases, the supercooling degree of the SSD/SPDD/H_2O/SMN phase change system first decreases and then increases. This may be because excessive SMN addition leads to agglomeration, reducing the number of nucleation sites. The sample with 3% SMN addition exhibits the lowest supercooling degree of 0.16 °C, and is used for subsequent research, denoted as SSD/SPDD/H_2O/SMN.

Figures 7e and 7f show the step cooling curve and DSC curve of SSD/SPDD/H_2O/SMN after 60 hot and cold cycles.

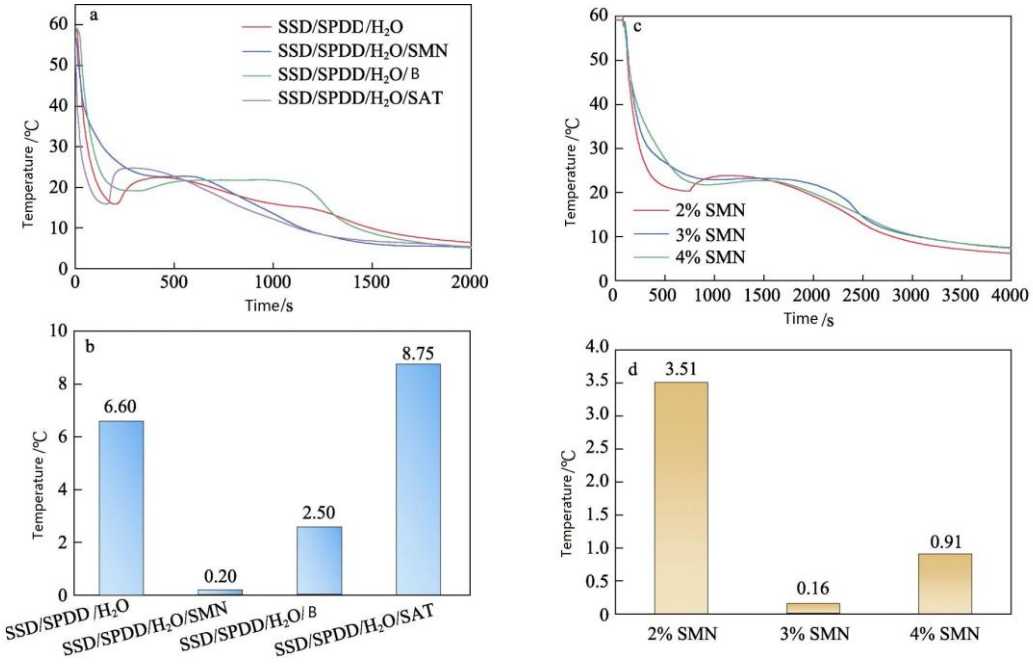

Figure 7 Step cooling curves (a) and subcooling degree (b) of SSD/SPDD/H_2O/SMN, SSD/SPDD/H_2O/borax, SSD/SPDD/H_2O/SAT phase transition systems; Step cooling curves (c) and subcooling degree (d) of SSD/SPDD/H_2O/SMN phase transition systems with 2%, 3% and 4% SMN addition amount; Step cooling curve (e) and DSC curves (f) of SSD/SPDD/H_2O/SMN after 60 hot and cold cycles

From Figure 7e, it can be seen that after 60 hot and cold cycles, the supercooling degree of SSD/SPDD/H_2O/SMN is 0.18 °C, showing little difference from the pre-cycle value of 0.16 °C, indicating good stability. As depicted in Figure 7f, the SSD/SPDD/H_2O/SMN system displayed an initial phase transition temperature of 26.50 °C and a latent heat of 174.10 J/g before thermal cycling. Following 60 heating–cooling cycles, the phase transition temperature marginally shifted to 26.60 °C, while the enthalpy declined to 170.70 J/g. The phase transition temperature continued to fall within the indoor thermal comfort envelope of 18–32 °C, and the retained latent heat remained above 170 J/g.

3.4 Preparation of Form-Stable Phase Change System

Agarose (AG) and locust bean gum (LBG), both naturally derived polysaccharides, are characterized by abundant hydroxyl functionalities and pronounced hydrophilic nature. The gelation mechanism underlying the agarose–locust bean gum composite hydrogel system is schematically depicted in Figure 8.

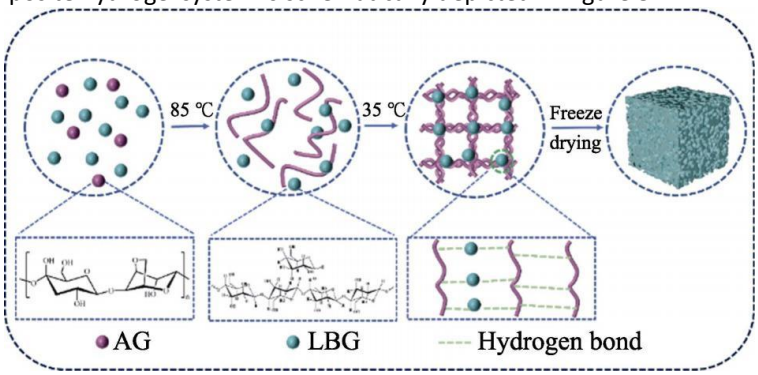

Figure 8 Schematic diagram of principle of compound gel

From Figure 8, it can be seen that based on its self-gelling property, AG exists as a random coil structure in high-temperature solutions. As the temperature decreases, the abundant hydroxyl groups in the AG side chains provide numerous hydrogen bonding and electrostatic interactions, causing AG chains to form double-helix

structures, which subsequently aggregate into bundles to form a gel [23]. After LBG is added, it acts as a thickener and stabilizer [24], playing a synergistic role in the AG gel formation process. Moreover, its long exposed mannose chain segments may form binding zones with the double-helix structure of AG [25], thereby improving the gel performance of AG. The SSD/SPDD/H_2O/SMN system is composited with the AG-LBG skeleton via impregnation, utilizing the hydrophilicity and rich porous structure of the skeleton to encapsulate the PCM, yielding the form-stable PCM.

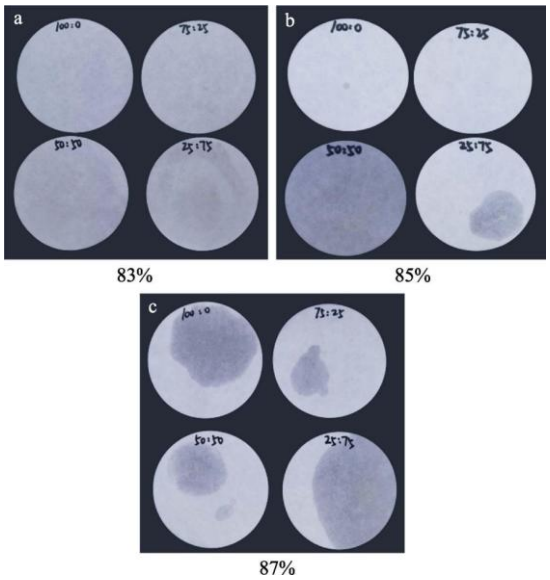

Figure 9 AG-LBG skeleton leak test results for PCM loads of 83% (a), 85% (b) and 87% (c)

Figure 9 shows the leakage test results of the SSD/SPDD/H_2O/SMN/AG-LBG form-stable PCM system.
From Figure 9, it can be seen that AG-LBG skeletons with PCM loadings of 83% (Figure 9a) and 87% (Figure 9c) both exhibit leakage. AG-LBG (50/50) and AG-LBG (25/75) with 85% PCM loading also show leakage. This may be because LBG itself lacks gelling properties; as its relative content increases, the sol viscosity rises, hindering the formation of AG double-helix structures, resulting in thinner gel pore walls and decreased gel strength [26]. The skeleton formed after freeze-drying is loose and exerts weak confinement on the PCM, leading to low load capacity. AG-LBG (100/0) with 85% PCM loading also shows slight leakage. This may be because pure AG gel has large pore sizes, and the impregnated PCM, with high fluidity, easily seeps out from the pores. Furthermore, due to the high brittleness of pure AG itself, the formed skeleton is prone to fracture. Only AG-LBG (75/25) with 85% PCM loading shows no leakage. This may be because the addition amount of LBG has a minimal hindering effect on gel formation, resulting in a complete gel structure, while alleviating the high brittleness issue of pure AG gel. Therefore, the final system SSPCM was selected as AG-LBG (75/25) with 85% PCM loading.
Figure 10 shows the leakage test results of SSD/SPDD/H_2O/SMN and SSPCM at different times.

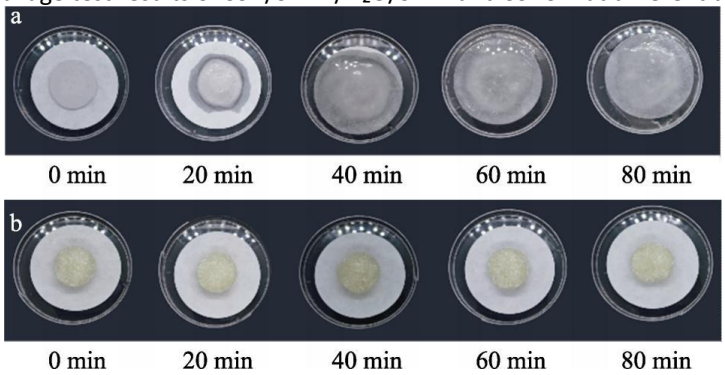

Figure 10 Test for leakage at different times of SSD/SPDD/H_2O/SMN (a) and SSPCM (b)

From Figure 10, it can be seen that SSD/SPDD/H_2O/SMN starts leaking after 20 min, while SSPCM shows no obvious leakage within 80 min, indicating that the AG-LBG skeleton [AG-LBG (75/25)] possesses good form-stabilizing effects and can alleviate the leakage problem of solid-liquid PCMs.

Figure 11 shows the SEM images of AG-LBG (75/25) and SSPCM.

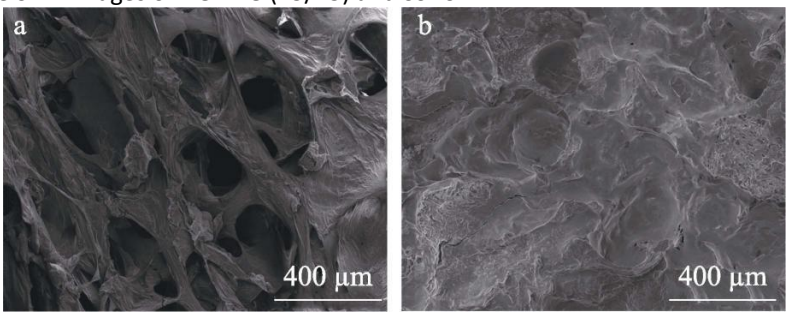

Figure 11 SEM images of AG-LBG (75/25) (a) and SSPCM (b)

From Figure 11, it can be seen that AG-LBG (75/25), serving as the supporting skeleton, possesses a rich porous structure (Figure 11a), providing sufficient space for adsorbing PCM. After impregnation, the PCM is uniformly adsorbed within the skeleton, and the skeleton surface becomes smooth with most pore structures disappearing (Figure 11b), indicating that the PCM is well fixed within the skeleton, providing a visual explanation for the leakage test results.

Figure 12 shows the step cooling curve and DSC curve of SSPCM.

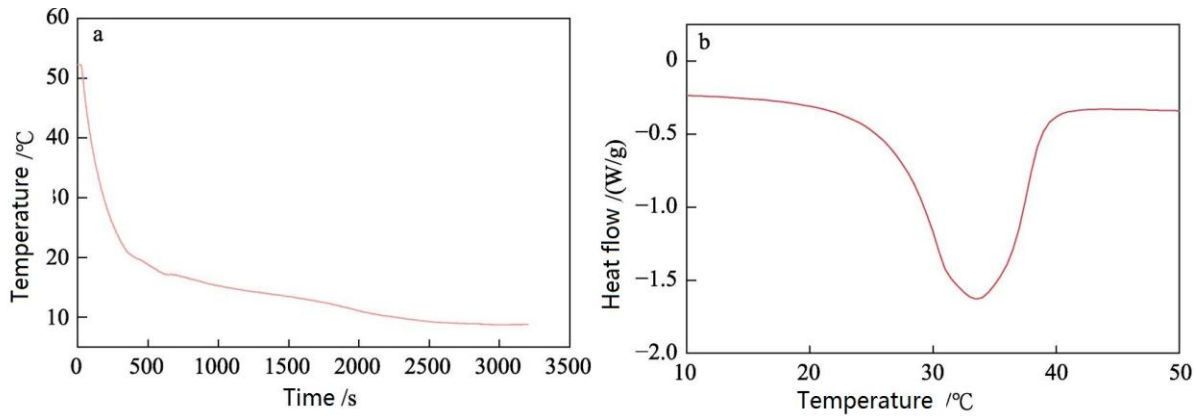

Figure 12 Step cooling (a) and DSC (b) curves of SSPCM

From Figure 12, it can be seen that SSPCM exhibits no obvious supercooling, and its supercooling degree is further reduced from 0.16 °C (for SSD/SPDD/H_2O/SMN) to 0 °C (Figure 12a). This phenomenon may be attributed to the AG-LBG (75/25) matrix, whose abundant porous architecture can furnish nucleation sites for the phase change material. The SSPCM exhibits a melting temperature of 26.40 °C and an enthalpy of fusion of 147.20 J/g. The experimentally determined phase transition temperature aligns closely with the theoretical prediction of 26.50 °C, whereas the measured enthalpy exhibits a minor discrepancy relative to the calculated value of 148 J/g. This discrepancy arises because the AG-LBG (75/25) matrix itself lacks phase transition properties, and the interfacial interactions between the supporting framework and the phase change material restrict its phase transition behavior, resulting in attenuated phase transition enthalpy.

3.5 Application Effect Analysis

In practical applications, the influence of PCM heat transfer rate on indoor temperature fluctuations in buildings needs to be considered. In the field of building insulation, materials with low thermal conductivity are typically required to reduce indoor-outdoor heat transfer rates, thereby improving indoor thermal comfort. Figure 13 presents the thermal conductivity characterization results for the SSD/SPDD eutectic salt, AG-LBG (75/25) composite gel, and the SSPCM formulation. As shown in Figure 13, the unmodified SSD/SPDD eutectic salt exhibits a relatively elevated thermal conductivity of 0.77 W/(m·K). By comparison, the AG–LBG (75/25) matrix, characterized by its porous architecture, demonstrates a substantially lower thermal conductivity of 0.08 W/(m·K). The SSPCM attains a thermal conductivity of 0.11 W/(m·K), which constitutes a marked decrease

compared with the pristine SSD/SPDD eutectic, thereby making it suitable for thermal insulation applications in building envelopes.

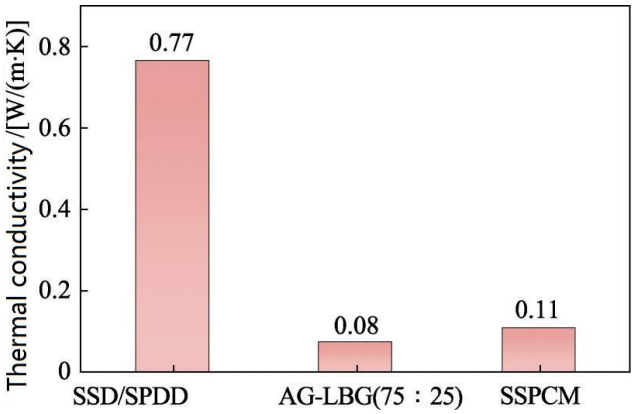

Figure 13 Thermal conductivity of SSD/SPDD salt mixture, AG-LBG (75/25) and SSPCM

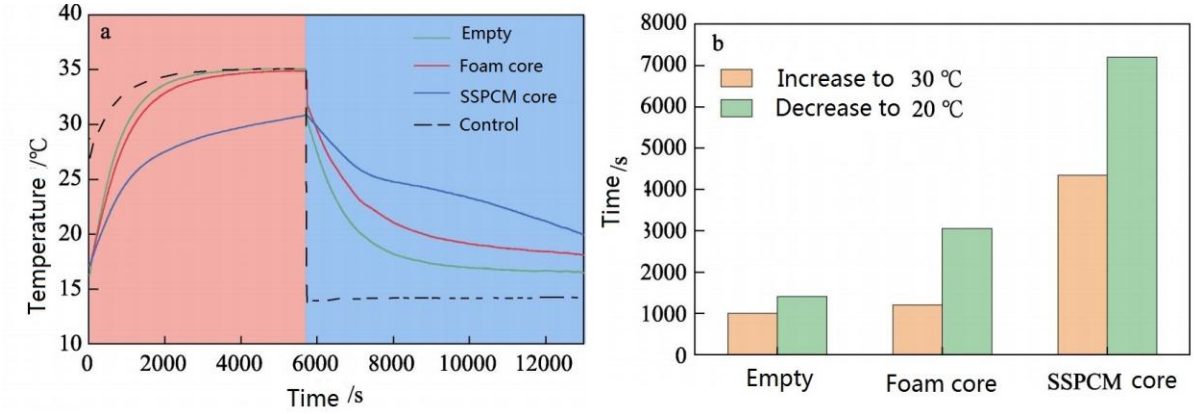

Figure 14 Heating and cooling test (a) and heating and cooling time (b) for empty container, foam sandwich and SSPCM sandwich

Figure 14 shows the simulated working condition test results.

From Figure 14, it can be seen that during heating under the same environment, the maximum internal temperatures of the empty container and foam sandwich both rise to approximately 35 °C, while the maximum internal temperature of the SSPCM sandwich is only 30.74 °C (Figure 14a), a decrease of approximately 4 °C compared to the former two. The times required for the empty container, foam sandwich, and SSPCM sandwich to heat up to 30 °C are 1000, 1204, and 4342 s, respectively. Compared with the foam sandwich, the heating time of the SSPCM sandwich increases by 2.60 times. The times required for the empty container, foam sandwich, and SSPCM sandwich to cool down from the maximum temperature to 20 °C are 1404, 3045, and 7203 s, respectively. The time required for the SSPCM sandwich is 2.37 times that of the foam sandwich, representing an extension of 1.37 times. The above results indicate that the SSPCM sandwich can significantly prolong the heating and cooling duration, effectively reducing indoor temperature fluctuations and demonstrating excellent thermal buffering performance.

4 Discussion

4.1 Thermodynamic Origins, Network Physics, and the Decoupling of Phase Stability from Leakage Control

The design logic underpinning the SSD/SPDD/AG-LBG system represents a decisive departure from the conventional trajectory of hydrated salt phase change material (PCM) research, where incremental improvements in supercooling suppression or thermal conductivity enhancement have historically been pursued as isolated objectives. To appreciate why this work achieves simultaneous breakthroughs across multiple performance axes, one must first revisit the thermodynamic origins of phase segregation and supercooling in

binary hydrated salt eutectics. In the SSD–SPDD system, phase separation is not merely a colloidal sedimentation problem; it is fundamentally rooted in the non-ideal solution behavior of multivalent anions in constrained crystallization water environments. Sodium sulfate decahydrate and sodium hydrogen phosphate dodecahydrate differ not only in anion geometry but also in hydration shell stability. Upon melting, SSD releases ten moles of structural water per formula unit, whereas SPDD liberates twelve. When physically blended, the transient oversaturation of sulfate and phosphate anions in the shared water pool generates localized ionic strength gradients that exceed the solubility limits of the denser residual salts, especially Na_2SO_4, which precipitates preferentially due to its lower coordination number with water molecules relative to HPO_4^{2-}. Traditional mitigation strategies—such as adding thickeners like xanthan gum or carboxymethyl cellulose—attempt to kinetically arrest this sedimentation through viscosity elevation, but they do not alter the underlying chemical potential imbalance. The innovation introduced here, namely the deliberate addition of 13 wt% extra water relative to the eutectic salt mass, operates instead on the thermodynamic level. By expanding the available solvent volume, the system shifts the saturation threshold of both salts outward, allowing previously insoluble residues to re-dissolve into fully solvated hydrated ions. This is not simply “dilution”; it is a controlled modulation of the activity coefficients of SO_4^{2-} and HPO_4^{2-} such that the eutectic melt remains homogeneous across repeated phase transitions. The persistence of phase stability after 100 thermal cycles, as demonstrated by the absence of stratification in Figure 6, confirms that this approach eliminates the driving force for segregation at its source, rather than masking it.

Supercooling, by contrast, arises from kinetic barriers to nucleation rather than thermodynamic instability. In hydrated salts, the challenge is exacerbated by the fact that crystallization must occur simultaneously with water reordering into the crystalline lattice. The selection of $Na_2SiO_3{\cdot}9H_2O$ as a nucleating agent is notable not only for its effectiveness but for what it reveals about lattice matching in hydrated salt systems. Classical nucleation theory posits that a nucleating agent must present a crystal plane with interatomic spacing closely aligned to that of the target crystallizing phase. Sodium silicate nonahydrate shares not only anionic similarity with the eutectic salts but also a comparable hydration number, meaning that its surface can template the ordered arrangement of both SO_4^{2-} and HPO_4^{2-} without inducing preferential crystallization of one component. This dual compatibility explains why SMN outperforms borax and sodium acetate trihydrate, both of which exhibit stronger lattice affinity to sulfate than to phosphate groups, thereby shifting the eutectic composition away from the desired 52:48 ratio during cycling. The step-cooling results, where SMN reduces supercooling from 6.60 °C to 0.16 °C, represent more than a numerical improvement; they demonstrate that nucleation can be rendered nearly barrierless under optimized conditions. Remarkably, the AG-LBG scaffold further eliminates even this residual supercooling, reducing it to 0 °C. This secondary suppression is not attributable to additional nucleation sites alone, but to capillary confinement effects within the polysaccharide network. When the SSD/SPDD/H_2O/SMN melt infiltrates the nanopores of the freeze-dried AG-LBG skeleton, the curvature of the liquid–solid interface alters the Gibbs free energy barrier for nucleation. In confined geometries, the critical nucleus radius decreases, making spontaneous crystallization more probable even under minimal undercooling. Thus, the system achieves a rare coupling: bulk thermodynamic stability through water modulation, and kinetic facilitation through hierarchical nucleation assistance.

The mechanical stabilization of the composite introduces yet another layer of complexity. Agarose and locust bean gum do not simply act as passive containers; their interaction defines the upper limit of PCM loading and determines long-term structural integrity. Agarose, as a thermoreversible gel, forms a double-helix architecture upon cooling, which aggregates into a three-dimensional network stabilized by hydrogen bonds. Locust bean gum, lacking intrinsic gelling ability, functions as a synergistic co-polysaccharide whose galactomannan chains interpenetrate the agarose helices, reinforcing the network through chain entanglement and secondary hydrogen bonding. The 75:25 AG:LBG ratio emerges as optimal precisely because it balances two opposing tendencies. Pure agarose yields large pores that accommodate high PCM volumes but suffer from brittleness and poor capillary retention, allowing leakage under thermal stress. Excess LBG, conversely, increases viscosity and disrupts helix formation, yielding a fragile, loosely connected scaffold incapable of withstanding repeated thermal expansion of the entrapped PCM. At 75:25, the composite achieves a pore size distribution narrow enough to exert capillary pinning forces on the molten salt hydrate while maintaining sufficient mechanical coherence to resist fracture. The SEM evidence, where impregnated SSPCM shows smoothed surfaces and occluded pores, visually corroborates this mechanism: the PCM is not merely adsorbed but structurally integrated into the polymer framework. Taken together, these findings reframe the design philosophy of form-stable PCMs—not as a search for better containers, but as the engineering of a thermodynamically coherent, kinetically facilitated, and mechanically interlocked multicomponent system.

4.2Benchmarking Against State-of-the-Art Systems, Thermal Transport Tradeoffs, and Building-Scale Energy Implications

To situate the SSD/SPDD/AG-LBG composite within the broader landscape of building-integrated thermal energy storage, it is essential to move beyond absolute performance metrics and examine normalized indicators that capture the interplay between latent heat, thermal conductivity, and operational temperature range. Over the past decade, hydrated salt PCMs have been extensively studied for indoor climate regulation, yet most systems remain trapped in a triad of compromises: high latent heat but severe supercooling, low leakage but insufficient phase change enthalpy, or excellent cycling stability but phase transition temperatures misaligned with human comfort. For example, Sang et al. achieved a 22.4 °C transition temperature in a $Na_2SO_4·10H_2O–Na_2CO_3·10H_2O$ eutectic, but required 3.2 °C of supercooling and relied on graphite additives to compensate for inherently low thermal conductivity. In contrast, the present system delivers a 26.4 °C melting point—squarely centered in the 18–32 °C comfort band—with negligible supercooling and a respectable 147.2 J/g latent heat despite the dilution effect of the supporting matrix. When benchmarked against recent literature, the SSPCM outperforms the majority of bio-polymer-based form-stable PCMs, where loadings rarely exceed 70 wt% and enthalpies typically fall below 120 J/g. The 85 wt% loading achieved here is particularly significant because it pushes the composite close to the theoretical maximum imposed by pore volume without sacrificing form stability, as evidenced by the 80-minute leak-free endurance at 50 °C.

Thermal conductivity presents a more nuanced picture. At 0.11 W/(m·K), the SSPCM is approximately seven times less conductive than the parent SSD/SPDD eutectic (0.77 W/(m·K)). While this reduction might initially appear disadvantageous, it is in fact strategically aligned with building envelope requirements. In wall or roof applications, excessively high thermal conductivity can undermine the buffering function of PCMs by allowing rapid heat penetration that bypasses the phase change process altogether. Low conductivity forces heat to dwell within the PCM layer during the day, maximizing the fraction of incident energy absorbed as latent heat rather than transmitted indoors. This design logic is validated by the thermal simulation results, where the SSPCM-sandwiched envelope delays heating to 30 °C by 2.60× relative to foam insulation and extends cooling duration by 1.37×. These factors translate directly into reduced HVAC cycling frequency, which in turn lowers compressor wear and electricity demand peaks. Importantly, the thermal lag introduced by the SSPCM does not create discomfort; because the phase change occurs within the comfort temperature window, indoor temperatures remain stable even as external conditions fluctuate. This distinguishes the material from high-conductivity PCMs infused with graphite or metal foams, which, while excellent for electronics cooling, are often suboptimal for passive building climate control where thermal resistance is desirable.

Another dimension worth discussing is the economic and environmental positioning of the system. Both agarose and locust bean gum are renewable, biodegradable polysaccharides with established supply chains in the food and pharmaceutical industries. Unlike synthetic polymers such as polymethyl methacrylate or polyvinyl alcohol, which dominate many commercial form-stable PCMs, AG and LBG introduce no persistent microplastics or toxic leachates. Sodium sulfate decahydrate and sodium hydrogen phosphate dodecahydrate are commodity chemicals available globally at low cost, and the addition levels of $Na_2SiO_3·9H_2O$ are minute (3 wt%), minimizing material expenses. Preliminary cost modeling suggests that at scale, the SSPCM could be produced for less than USD 8–10 per kilogram, competitive with conventional expanded polystyrene insulation when amortized over a 20-year building lifecycle. Furthermore, the absence of flame retardants or volatile organic compounds enhances its suitability for green building certifications such as LEED or BREEAM. From a lifecycle perspective, the system's ability to reduce annual heating and cooling loads by delaying temperature excursions directly translates into avoided CO_2 emissions, potentially offsetting the embedded energy of its production within the first 2–3 years of operation. These systemic advantages underscore why the SSPCM is not merely a laboratory curiosity but a viable candidate for real-world deployment in residential and light-commercial construction.

4.3 Limitations, Unresolved Physicochemical Interactions, Scalability Challenges, and Forward-Looking Research Trajectories

Despite its compelling performance profile, the SSD/SPDD/AG-LBG system is not without limitations, and a candid appraisal of these constraints is essential for guiding future research. One of the most pressing issues is the intrinsic hysteresis between melting and crystallization temperatures introduced not by supercooling but by the thermal inertia of the AG-LBG matrix. Although the step-cooling tests report zero supercooling, full-scale building applications involve slow, diurnal temperature ramps rather than abrupt quenches. Under such quasi-static conditions, the polymer scaffold may delay heat release, shifting the effective cooling benefit toward

later hours and potentially mismatching occupancy patterns. This temporal decoupling has not yet been quantified in multi-day cycling tests, which represent the next logical validation step. Additionally, while 60 thermal cycles demonstrate excellent stability, building envelopes are expected to endure hundreds, if not thousands, of cycles over decades. Prolonged exposure could lead to subtle recrystallization of SSD or SPDD at the polymer–salt interface, gradually degrading pore confinement and increasing leakage risk. Accelerated aging under combined thermal and humidity stress is therefore necessary to establish true longevity.

A second area requiring deeper investigation is the interfacial interaction between the hydrated salt eutectic and the polysaccharide hydroxyl groups. FTIR and XRD data confirm that the composite is physically blended rather than chemically bonded, yet the DSC enthalpy of SSPCM (147.2 J/g) is slightly lower than the theoretical value expected from 85 wt% loading of the eutectic. This suggests that a fraction of the PCM is either spatially constrained or experiences altered hydrogen bonding environments that suppress full phase transition. Molecular dynamics simulations could elucidate whether water molecules in the eutectic preferentially coordinate with AG-LBG hydroxyls, effectively reducing the free water available for latent heat exchange. If confirmed, this insight could guide post-treatment strategies—such as mild crosslinking or surface hydrophobization—to minimize parasitic interactions without compromising form stability.

Scalability introduces its own set of engineering hurdles. The current synthesis relies on freeze-drying to generate the AG-LBG scaffold, a process that is energy-intensive and difficult to scale economically for large-volume building materials. Alternative scaffold fabrication methods, such as ambient-pressure drying or solvent exchange, merit exploration to reduce embodied energy. Similarly, the impregnation step, while effective at laboratory scale, may prove challenging for continuous manufacturing lines. Roll-to-roll or vacuum-assisted infiltration techniques borrowed from battery electrode production could offer viable pathways, but would require precise control of melt viscosity and pore wetting dynamics. Fire safety also warrants attention: although hydrated salts themselves are non-flammable, the organic polysaccharide matrix introduces combustible content. Standard fire retardancy tests (e.g., UL-94 or cone calorimetry) should be conducted, and if necessary, eco-friendly flame-retardant additives compatible with the eutectic chemistry should be identified.

Looking forward, the design principles demonstrated here open multiple tangential research avenues. The concept of using excess water to suppress phase segregation could be extended to other problematic eutectic systems, such as chloride-based salts for low-temperature refrigeration. The AG-LBG scaffold, with its abundance of hydroxyl groups, could be functionalized to carry hygroscopic salts for simultaneous thermal and moisture buffering—a highly desirable trait in humid climates. Moreover, the near-elimination of supercooling suggests that this system could serve as a calibration benchmark for nucleation models in hydrated salt research. Finally, integration with active building systems—such as photovoltaic panels or night-ventilation cooling—could transform the SSPCM from a passive insulator into a dynamic energy management node. In sum, while the present work conclusively demonstrates a high-performance, low-cost, and environmentally benign form-stable PCM, its full realization as a mainstream building material will depend on addressing these physicochemical, manufacturability, and lifecycle challenges in the next generation of studies.

5 Conclusion

A novel form-stable PCM (SSPCM) for building insulation applications was prepared via the impregnation method.

(1) The SSD/SPDD mixed salt prepared via physical composite with m(SSD):m(SPDD)=52:48 exhibits a phase transition temperature of 28.90 °C and a phase transition enthalpy of 216.40 J/g.

(2) The SSD/SPDD/H_2O/SMN phase change system prepared with 13% water addition and 3% SMN addition displays the lowest supercooling degree of 0.16 °C, which remains at 0.18 °C after 60 hot and cold cycles.

(3) The SSPCM, employing AG–LBG (75/25) as the supporting matrix with a PCM loading of 85%, exhibited no leakage for 80 min. Its phase transition temperature, latent heat, and thermal conductivity were determined to be 26.40 °C, 147.20 J/g, and 0.11 W/(m·K), respectively.

(4) Compared with the foam sandwich, the heating time of the SSPCM sandwich increases by 2.60 times, and the cooling time extends by 1.37 times.

The SSPCM developed in this investigation effectively attenuates indoor temperature variations, demonstrating promising applicability for building thermal insulation applications.

References

[1] Xiang B, Cao X L, Yuan Y P, et al. A novel hybrid energy system combined with solar-road and soil-regenerator: Sensitivity analysis and optimization. Renewable Energy, 2018, 129: 419–430.

[2] He Z X, Li M M, Li Y H, et al. Electrospun nitrogen-doped carbon nanofiber as negative electrode for vanadium redox flow battery. Applied Surface Science, 2019, 469: 423–430.

[3] Shah T R, Ali H M. Applications of hybrid nanofluids in solar energy, practical limitations and challenges: A critical review. Solar Energy, 2019, 183: 173–203.

[4] Devaux P, Farid M M. Benefits of PCM underfloor heating with PCM wallboards for space heating in winter. Applied Energy, 2017, 191: 593–602.

[5] Ma Y Q, Wang H C, Zhang L, et al. Flexible phase change composite films with improved thermal conductivity and superb thermal reliability for electronic chip thermal management. Composites Part A: Applied Science and Manufacturing, 2022, 163: 107203.

[6] Tao J L, Luan J D, Liu Y, et al. Technology development and application prospects of organic-based phase change materials: An overview. Renewable and Sustainable Energy Reviews, 2022, 159: 112175.

[7] Huang X B, Chen X, Li A, et al. Shape-stabilized phase change materials based on porous supports for thermal energy storage applications. Chemical Engineering Journal, 2019, 356: 641–661.

[8] Xi S B, Bu Z, Kong G, et al. Perspectives on the application of phase change energy storage in building energy efficiency. ES Energy & Environment, 2022, 16: 1–3.

[9] Hao Y P, Liu L, Zhang Y A, et al. Preparation and properties of electrically driven PEG/EG composite phase change materials. Fine Chemicals, 2022, 39(3): 513–518.

[10] Aftab W, Huang X Y, Wu W H, et al. Nanoconfined phase change materials for thermal energy applications. Energy & Environmental Science, 2018, 11(6): 1392–1424.

[11] Wu M Q, Wu S, Cai Y F, et al. Form-stable phase change composites: Preparation, performance, and applications for thermal energy conversion, storage and management. Energy Storage Materials, 2021, 42: 380–417.

[12] Li T X, Wu M Q, Wu S, et al. Highly conductive phase change composites enabled by vertically-aligned reticulated graphite nanoplatelets for high-temperature solar photo/electro-thermal energy conversion, harvesting and storage. Nano Energy, 2021, 89(Part A): 106338.

[13] Yu K Y, Liu Y S, Yang Y Z. Review on form-stable inorganic hydrated salt phase change materials: Preparation, characterization and effect on the thermophysical properties. Applied Energy, 2021, 292: 116845.

[14] Chen Z B, Zhang X L, Ji J, et al. A review of the application of hydrated salt phase change materials in building temperature control. Journal of Energy Storage, 2022, 56(Part C): 106157.

[15] Wu Y N, Wang X, Tang B T, et al. Preparation and properties of long chain alkyl eutectic phase change materials. Fine Chemicals, 2021, 41(7): 1504–1510.

[16] Man X, Lu H, Xu Q, et al. Review on the thermal property enhancement of inorganic salt hydrate phase change materials. Journal of Energy Storage, 2020, 72(Part E): 108699.

[17] Xie N, Luo J M, Li Z P, et al. Salt hydrate/expanded vermiculite composite as a form-stable phase change material for building energy storage. Solar Energy Materials and Solar Cells, 2019, 189: 33–42.

[18] Sang G C, Zeng H N, Guo Z Q, et al. Studies of eutectic hydrated salt/polymer hydrogel composite as form-stable phase change material for building thermal energy storage. Journal of Building Engineering, 2022, 59: 105010.

[19] Wang X, Li Z C, Wu Y N, et al. Preparation and application of $Na_2CO_3·10H_2O$-$Na_2HPO_4·12H_2O/SiO_2$ composite shape-stabilized phase change materials. Fine Chemicals, 2021, 41(3): 623–629, 656.

[20] Tang Y R, Gao D L, Guo Y F, et al. Supercooling and phase separation of inorganic salt hydrates as PCMs. Applied Mechanics and Materials, 2011, 71–78: 2602–2605.

[21] Kalidasan B, Pandey A K, Rahman S, et al. Experimental investigation of graphene nanoplatelets enhanced low temperature ternary eutectic salt hydrate phase change material. Energies, 2020, 16(4): 1574.

[22] Kalidasan B, Pandey A K, Saidur R, et al. Expanded graphite intersperse reliable binary eutectic phase change material for low temperature thermal regulation systems. Materials Today Sustainability, 2020, 24: 100602.

[23] Cao L. Preparation of agarose-based hydrogel and its application in soilless culture. Suzhou: Soochow University, 2022.

[24] Zhang Y A, Zang Z, Lu R W, et al. Repeatable instantaneous chromogenic and magnetic-responsive hydrogels based on an agarose-locust bean gum network. Industrial & Engineering Chemistry Research, 2021, 63(3): 1442–1450.

[25] Viebeke C, Piculell L. Adsorption of galactomannans onto agarose. Carbohydrate Polymers, 1996, 29(1): 1–5.
[26] Sun C, Liu X. Synergistic interaction between agar and locust bean gum and its slow release property of gel framework material. China Food Additives, 2020, 31(5): 75–81.